On the Feasibility of Out-of-Band Spatial Channel Information for Millimeter-Wave Beam Search

Pekka Kyösti, Peize Zhang, *Member, IEEE*, Aarno Pärssinen, *Senior Member, IEEE*, Katsuyuki Haneda, *Member, IEEE*, Pasi Koivumäki, *Member, IEEE*, and Wei Fan, *Senior Member, IEEE*

***Abstract*— Prolonged beam alignment is the main source of overhead in mobile wireless communications at millimeter-wave (mm-wave) frequencies due to narrow beams following the requirement of high antenna gains. Out-of-band spatial information may be used in initial beam search when lower-frequency-band radios are operating in conjunction with mm-wave radios. The feasibility of using low-band channel information for coarse estimation of high-band beam directions strongly depends on the spatial congruence between the two frequency bands. In this work, we try to answer two related questions. First, how similar is the power angular spectrum (PAS) of propagation channels between two widely separated frequency bands? Then, what is the impact of practical antenna configurations on spatial channel similarity? We propose a beam directions-based metric to assess the power loss and the number of false directions if out-of-band spatial information is used instead of in-band information. This metric is more practical and useful than comparing the PASs directly. Point cloud ray-tracing and propagation measurement results across multiple frequency bands and environments are used to show that the degree of spatial similarity of beamformed channels is related to antenna beam widths, frequency gap, and radio link conditions.**

***Index Terms*— Beam search, millimeter-wave, radio channel, spatial channel similarity.**

I. Introduction

As THE global adoption of 5G technology continues, next-generation wireless communication systems, that is, B5G/6G are expected to provide ultrahigh throughput and seamless connectivity in coexisting sub-6-GHz and millimeter-wave (mm-wave) cellular networks [1]. Following the reasoning and definitions of [2], we divide the mm-wave radio frequency (RF) as the lower region, 30–100 GHz, and the upper region, 100–300 GHz, and name them the lower and the upper mm-wave band, respectively. The transmission loss increases with increasing frequency and, typically, higher antenna gains are used to compensate for the losses. A few dBi might not be sufficient anymore, but antenna gains of even a few tens of decibels might be needed at the upper mm-wave RF [3]. The gain may be realized by, for example, high-gain antenna elements, lens structures, phased arrays, or combinations of these [3]. Here, we assume flexible beam steering capability and hence phased arrays.

From the propagation analysis perspective, high-capacity mm-wave cellular communications will likely offer up to a few hundred meters of directed coverage [4], [5]. Supported link distances become substantially shorter in nonline of sight (NLOS) scenario [6], [7], because of severe path loss and sensitivity to blockage due to obstacles. Apart from the frequency and distance-dependent free space path loss, also the losses related to diffraction and material penetration strongly increase with increasing frequency [8], while the reflection coefficients are rather constant across sub-6-GHz and mm-wave frequencies. Attenuation of paths due to shadowing by obstacles becomes stronger at higher RF. The probability of blockage, on the one hand, may increase, since with shorter wavelengths, the Fresnel zone becomes smaller and even smaller obstacles may block the path. While, on the other hand, smaller openings between obstacles are needed to keep smaller Fresnel zones nonobstructed [2]. Another type of blocking of signals, that is, interference by other radio sources, will be less severe due to more directive antennas and focused beams.

Higher antenna gain means practically more directivity and narrower beams of radiation patterns. Initialization of a communication link with transceivers relying on adaptive high-gain antenna systems necessitates a beam search procedure [9]. A high-gain antenna, forming a narrow beam, is susceptible to loss of signal, leading to a more laborious beam search scheme [10]. Overall, the higher the RF, the more carefully narrow antenna beams must be directed and the more frequently severe blockage events will occur, especially if antennas are at low height and there is motion either by transceivers or the environment. Sub-6-GHz radio systems can establish more flexible and reliable communication links with continuous coverage, when compared to mm-wave systems. Coming B5G/6G transceivers are foreseen to support multiband transmission across a wide set of frequencies. Therefore,

Manuscript received 17 October 2022; revised 1 February 2023; accepted 15 February 2023. Date of publication 3 March 2023; date of current version 5 May 2023. This work was supported in part by the European Commission through the H2020 Project Hexa-X under Grant 101015956 and in part by the 6G Flagship Program through the Academy of Finland under Grant 346208. *(Corresponding author: Pekka Kyösti.)*

Pekka Kyösti is with the Centre for Wireless Communications, University of Oulu, 90570 Oulu, Finland, and also with the Keysight Technologies Finland Oy, 90630 Oulu, Finland (e-mail: pekka.kyosti@oulu.fi).

Peize Zhang and Aarno Pärssinen are with the Centre for Wireless Communications, University of Oulu, 90570 Oulu, Finland (e-mail: peize.zhang@oulu.fi; aarno.parssinen@oulu.fi).

Katsuyuki Haneda and Pasi Koivumäki are with the Department of Electronics and Nanoengineering, Aalto University, 02150 Espoo, Finland (e-mail: katsuyuki.haneda@aalto.fi; pasi.koivumaki@aalto.fi).

Wei Fan is with the Antenna, Propagation and Millimeter-Wave Systems Section, Department of Electronic Systems, Faculty of Engineering and Science, Aalborg University, 9220 Aalborg, Denmark (e-mail: wfa@es.aau.dk).

Color versions of one or more figures in this article are available at https://doi.org/10.1109/TAP.2023.3249837.

Digital Object Identifier 10.1109/TAP.2023.3249837

it is attractive to reuse available out-of-band spatial channel information for higher frequency beam steering and alignment with reduced training overhead [11], [12], that is, extracting easily available coarse angular information with low-frequency antenna systems and using it to initialize beam search at the higher frequency. This is motivated by findings of multiband measurements, for example, the ones described in [13] at 6, 30, and 60 GHz, indicating that there can be a substantial similarity in directions of strong propagation path components across radio frequencies.

The radio channel contains both the propagation channel and antennas, that is, transceivers always see the channel through antennas. Even though dominant propagation paths are often similar at separate frequencies [2], the antenna systems are not. The physical size of transceivers and antenna structures limits the aperture and consequently the achievable electrical size and directivity of antennas. Systems equipped with larger antenna arrays at higher RF have typically much higher angular resolution and are capable of obtaining finer granularity information of, for example, directions of multipath components. Therefore, out-of-band information of the radio channel may not differ only due to the differences in wave propagation, but also due to differences in antennas employed in two frequency bands. To this end, our primary task is to explore how similar the propagation channels are at separate frequency bands and how much useful spatial channel information one band can provide to the other. It is also essential to consider practical antenna size limitations when leveraging low-band spatial channel information for high-band beam search.

Frequency dependence of channel parameters has been a topic of interest in the standardization of wave propagation and channel models for many years [14]. Extensive empirical analyses of indoor and outdoor spatial channels have been promoted in literature, where measured power angular delay profiles (PADPs) are presented and compared over multiple frequencies from microwave to mm-wave bands [13], [15], [16], [17], [18], [19]. Analysis of directional propagation channels reveals that similar dominant paths can be observed in different frequency bands, yet many more weak multipath components (MPCs) can be detected in lower bands when compared to the higher bands. Meanwhile, it is clear that spatial profiles at mm-wave bands tend to be more specular and sparse. A method proposed in [15] performs rough and quick angle estimation at a lower frequency and reuses the estimated spatial profiles for precious beam operation at high frequency, considering the high similarity of spatial profiles between low- and high-frequency bands. In [20], channel sounding results reported in the mmMAGIC project, covering different propagation scenarios and different frequency bands in 2-86 GHz [21], were summarized with the focus on the statistical analysis of delay dispersion parameters. Though multiband channel similarity can be directly observed, there is a lack of metrics to characterize the degree of it. In [22], a multipath similarity index was proposed to measure temporal channel similarity by comparing multiband power delay profiles (PDPs). To the best of our knowledge, however, no definite metric has been proposed to measure the spatial channel similarity in terms of power angular spectrum (PAS).

In this context, this article provides the following specific contributions.

1) Two metrics for the evaluation of spatial channel similarity at two different frequencies are developed under practical antenna pattern constraints, where one offers a probability measure on the total variation distance of PAS, while the other offers a more practical and intuitive scheme to identify the available beam directions. Compared with existing multifrequency propagation studies, we not only provide a visual comparison of site-specific spatiotemporal channel characteristics across different frequencies, but also propose quantitative metrics to characterize the spatial similarity level of radio channels.
2) To conduct statistical analysis, a sufficiently large amount of multiband propagation channel data at the same transmitter (Tx) and receiver (Rx) locations have been collected. We use point clouds ray tracing, which is an attractive approach given the difficulty of conducting extensive channel measurement campaigns consisting of thousands of locations. In addition, dual-band channel-sounding data from a few environments are utilized for validation. A fair comparison of multiband spatial channel characteristics can be performed at identical Tx–Rx settings.
3) Statistical analysis of multiband spatial channel similarity using our proposed metrics provides valuable insights into the feasibility of out-of-band spatial channel information for mm-wave beam steering and alignment. The usefulness of lower band channel information for mm-wave beam search will change depending on the system configurations, such as antenna configurations, channel line of sight (LOS) condition, and beam direction estimation methods.

The remainder of this article is organized as follows. Section II introduces the propagation data obtained by point cloud ray-tracing simulations and channel measurements across multiple frequency bands and environments. Section III describes two proposed metrics to measure the spatial channel similarity based on the multiband PAS. Section IV discusses the feasibility of lower frequency spatial channel information-aided mm-wave beam search using practical antenna configurations and Section V concludes the article.

II. Multiband Propagation Channel Data Collection

In Section II, we briefly describe propagation data analyzed in Sections III and IV.

A. Point Cloud Ray-Tracing Simulations

The propagation channel data used in this work is generated via ray-tracing simulations in applying a laser-scanned point cloud model of the Helsinki-Vantaa airport check-in area at Terminal 2 [23], [24]. The raw point cloud is obtained with

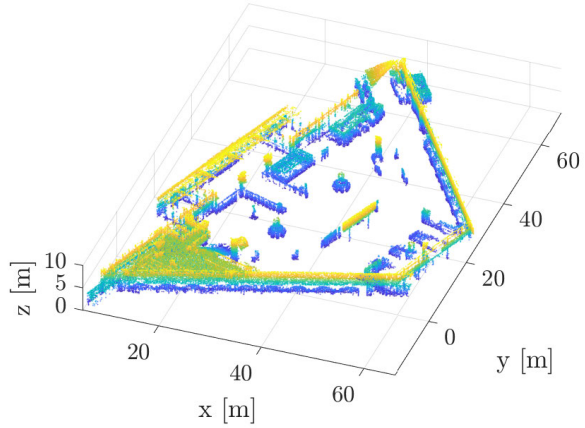

(a)

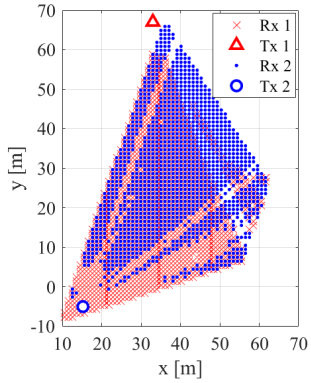

(b)

Fig. 1. (a) Laser-scanned point cloud used in ray tracing, where the points are colored according to their position on the z-axis. (b) Tx and Rx positions.

a Z+F IMAGER[1] 5006-h 3-D laser scanner [25], which uses movable mirrors to steer a laser beam in different directions to detect the distances to reflective surfaces. The point cloud used in ray-tracing simulations is illustrated in Fig. 1(a). Note that the raw point cloud is preprocessed by removing the ceiling of the airport terminal (i.e., points above 10 m), as well as the floor, which will significantly reduce the total number of points for ray-tracing simulations. Other clutters, for example, pedestrians that were present during the laser scanning, are removed so that the ray-tracing simulations were performed without any human presence in the hall. The points that represent the walls of the airport terminal, check-in kiosks, and other fixtures of the environment are kept during ray-tracing simulations. As shown in Fig. 1(b), two Tx locations are selected, where Tx1 is in a side corridor and Tx2 is behind the stairs in the check-in area. Two Rx sets are selected, including thousands of Rx locations, to establish communication links to Tx1 and Tx2, respectively. Propagation data contains in total 2875 links, composed of 1473 links between Tx1 and Rx1 and 1402 links between Tx2 and Rx2. It can be observed that Rx locations are not fully uniform since certain sectors with direct paths to the corresponding Rx locations are excluded. Thus, only NLOS links are considered during the simulation, while line-of-sight (LOS) links are all blocked by physical objects.

[1]Registered trademark.

TABLE I
RAY-TRACING SIMULATION PARAMETERS

Frequency [GHz]	4	15	28	60	86
Permittivity	4.3	4.2	3.9	3.6	3.3
Shadowing loss [dB]	20	30	60	100	130

(a) (b)

Fig. 2. Channel measurement campaigns in (a) indoor corridor and (b) entrance hall.

As regards the ray-tracing simulation setup, the following propagation mechanisms are considered in the simulations, including single- and double-bounce paths, diffracted paths, and diffraction to single- and double-bounce paths. A total of five frequency bands (i.e., 4, 15, 28, 60, and 86 GHz) are considered. The permittivity of the environment and shadowing losses for each frequency, which were used in the ray-tracing simulations, are summarized in Table I. These parameters are optimized based on the channel measurement campaign conducted at the airport [26] following the methodology outlined in [21]. Note that the measured or optimized parameters were not available at 4 GHz, and they were obtained using a linear fit according to the available parameters in other bands. The permittivity of the physical objects in the environment is assumed to be identical for simplicity of the measurement-based calibration and is used to calculate reflection and diffraction coefficients. A flat shadowing loss, originally estimated from field measurement data, is applied to the rays that are *shadowed*, that is, whose first Fresnel ellipsoid is not free of obstructions [27], [28].

B. Channel Measurement Campaigns

Channel measurements in two indoor scenarios (see Fig. 2) were performed at Aalborg University, Denmark. A long-range vector network analyzer (VNA)-based channel sounding system enabled by radio over fiber (RoF) technology was employed for the measurements. The details about the channel sounder at 28 GHz can be found in [29]. In [30], a long-range channel sounder at 220–330 GHz was reported. The same concept is employed for the 100-GHz channel sounder utilized in our measurement, except that different frequency extenders are used. For both channel measurements, omnidirectional antennas were used at the Tx side, while directional antennas were employed at the Rx side to cover 360° in the azimuth domain. A directional channel sounding scheme was employed at the Rx side to measure the spatial channel profile directly with the help of the turntable. Note that directional antennas

TABLE II
ANTENNA CONFIGURATIONS FOR DUAL-BAND CHANNEL MEASUREMENTS

Envi.	Indoor corridor		Entrance hall	
Freq. range [GHz]	28–30	99-101	28–30	99-101
Freq. point	1001		1001	601
Tx ant. type	Omni.			
Rx ant. type	Horn			
Rx ant. height [m]	0.93	1.25	1.25	
Rx ant. HPBW [deg]	40	40	20.8	16
Rx ant. Gain [dBi]	13.5	13.5	19.5	20.5
Rx rot. Step [deg]	1.5	1	8	8

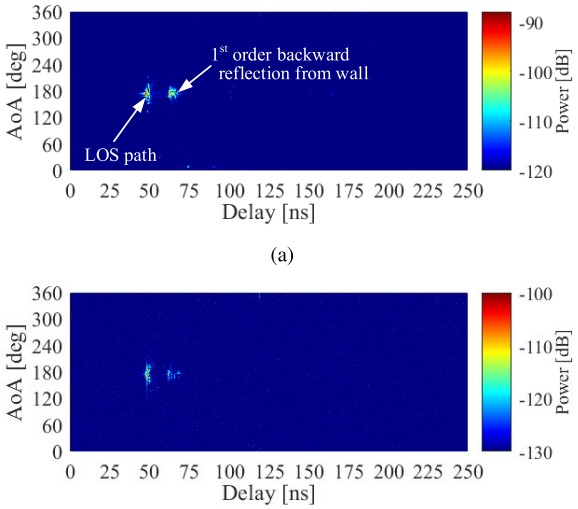

Fig. 3. Measured PADPs in the indoor corridor at (a) 28 and (b) 100 GHz.

with similar half power beamwidth (HPBW) were employed to ensure that channel spatial profiles at different frequency bands are not affected by the antenna pattern. The measured PADPs is estimated based on the method proposed in [31], which can be further used to extract MPCs with peak detection algorithm. A dynamic range of 30 dB is set in the measurement results.

Only one LOS link in each environment was selected due to highly time-consuming measurements. For the indoor corridor scenario, a measurement bandwidth of 2 GHz with 1001 frequency points was set in the VNA, resulting in a delay resolution of 0.5 ns and a maximum excess delay of 500 ns. The measurement distance was set to 14 m. The measured PADPs at 28 and 100 GHz are shown in Fig. 3. The measured channels are highly sparse and specular, and the same dominant paths along LOS directions can be identified at two frequencies. For the entrance hall scenario, 1001 and 601 frequency points were selected with the same sounding bandwidth of 2 GHz at 28 and 100 GHz, respectively. The measurement distance was set to 4.84 m. The details of antenna configurations are summarized in Table II.

C. Multipath Channel Characterization

Outputs of the ray-tracing and channel measurements include all captured MPCs within a specific power range. Each

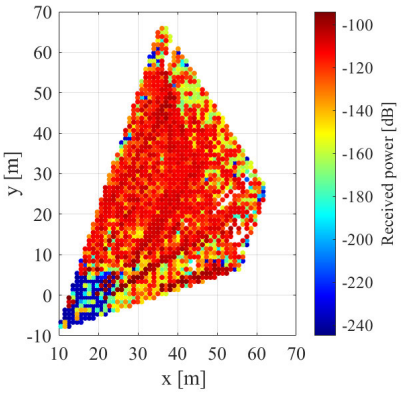

Fig. 4. Total channel gain in each Rx position at 86 GHz.

MPC is characterized by its received power, propagation delay, angle of arrival (AoA), and angle of departure (AoD) (when available). In the single-directional case, the discrete PADP can be written as $P(q;\Omega,\tau)$, where q denotes the index for the link, that is, for the Tx and Rx locations, Ω denotes the AoA, and τ denotes the propagation delay. In this article, we only analyze the spatial channel similarity on the Rx side only, but the same applies to the Tx side as well, since Tx and Rx were deployed similarly. For the sake of simplicity, we use subscripts L and U to denote the lower- and upper-frequency antenna systems, propagation channels, and their parameters, respectively. Consequently, each PADP can be represented as a sum of discrete paths $p = 1, \ldots, l$ as

$$\begin{cases} P_L(\Omega,\tau) = \sum_{p=1}^{l_L} P_{L,p}\,\delta\big(\Omega-\Omega_{L,p}\big)\,\delta\big(\tau-\tau_{L,p}\big) \\ P_U(\Omega,\tau) = \sum_{p=1}^{l_U} P_{U,p}\,\delta\big(\Omega-\Omega_{U,p}\big)\,\delta\big(\tau-\tau_{U,p}\big) \end{cases} \tag{1}$$

Where the link index q is left out for brevity, $\delta(\cdot)$ is the delta function, l is the total number of rays, P_p, Ω_p, and τ_p are the received power,[2] AoA, and propagation delay of the pth rays, respectively.

Fig. 4 shows the total channel gain of each link at 86 GHz, which is calculated as the sum of channel gains of paths $\sum_{p=1}^{l} P_p$. A significantly large variation of close to 140 dB in channel gains among different Rx positions can be observed. Discrete PADPs of a specific link at 4 and 86 GHz are shown in Fig. 5, where the circles and triangles represent paths in low and high bands, respectively. In terms of the power difference, P_p at lower frequencies are much larger than those at higher frequencies as indicated in Fig. 5(a). It is a bit difficult to explore the channel similarity visually without power normalization. On the other hand, from the top view of 3-D PADP [see Fig. 5(b)], dominant rays across two frequencies share similar propagation delays and AoAs. Since our focus in this work is on angular aspects, we reduce PADPs to PASs and mainly treat angular power distributions henceforth.

[2]We assume unity transmit power and use *received power* and *channel gain* interchangeably.

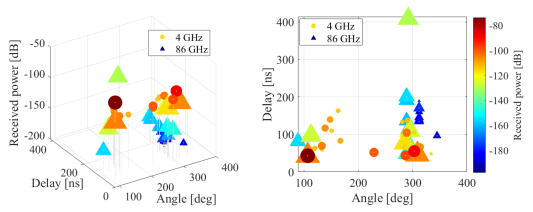

Fig. 5. Comparison of the PADPs at 4 and 86 GHz for link 15. (a) 3-D plot. (b) Top view.

III. Spatial Channel Similarity Metrics

In this section, two metrics used for measuring the spatial channel similarity are proposed based on the multiband propagation channel data. The first method applies the widely known total variation distance of probability measures on the PAS estimated over different frequency bands. The second method is more practical. There we assume certain antenna beam widths at different frequencies and try to directly evaluate the usability of spatial channel information extracted at one frequency for the beam search at the other frequency. Following the definitions of the two metrics, the comparison study has been conducted across different frequency combinations and methods.

A. PAS Similarity Percentage

An intuitive view of multiband spatial channel similarity is to directly compare measured PASs. However, a direct comparison of possibly discrete and sparse PASs is difficult. Hence, we develop a metric, the so-called PAS similarity percentage (PSP), to measure the total variation distance of normalized PASs. According to procedures reported in [32], the continuous PAS is first estimated by filtering the actual power angular distributions of the propagation channel by a function that corresponds to a limited aperture of an antenna. The filtering is performed for both of the considered frequencies. Then, both spectra are normalized to the sum power of unity such that they can be interpreted as probability distribution functions (PDFs). Finally, the total variation distance between the probability distributions, that is, normalized PASs is calculated.

1) Beam Filtering: Any antennas or arrays can be used for defining the angular filter. It can be, for example, a phased array, and the filtering operation would equal the classical Bartlett beamforming. Here, a simple synthetic radiation pattern $G(\Omega)$ specified by the 3rd Generation Partnership Program (3GPP) in [14, Table 7.3-1] is adopted. As shown in Fig. 6, the peak to minimum gain ratio is 30 dB, and 10° is chosen as the definable HPBW $\theta_{3\ \mathrm{dB}}$. We take convolution $\int P(\Omega)\, G(\alpha-\Omega)d\Omega$ of the propagation channel PAS $P(\Omega)$ and the angular filter $G(\Omega)$. This corresponds to steering the beam to a direction α and collecting the sum power from all observable MPCs weighted with corresponding beam gains. The resulting power with steering angle α is

$$\begin{cases} B_L(\alpha) = \displaystyle\sum_{p=1}^{l_L} P_{L,p}\, G\big(\alpha-\Omega_{L,p}\big) \\ B_U(\alpha) = \displaystyle\sum_{p=1}^{l_U} P_{U,p}\, G\big(\alpha-\Omega_{U,p}\big). \end{cases} \tag{2}$$

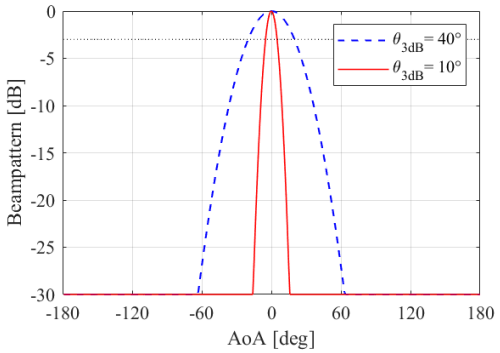

Fig. 6. Normalized gain pattern of the 3GPP beam with $\theta_{3\ \mathrm{dB}} = 10°$ and 40°.

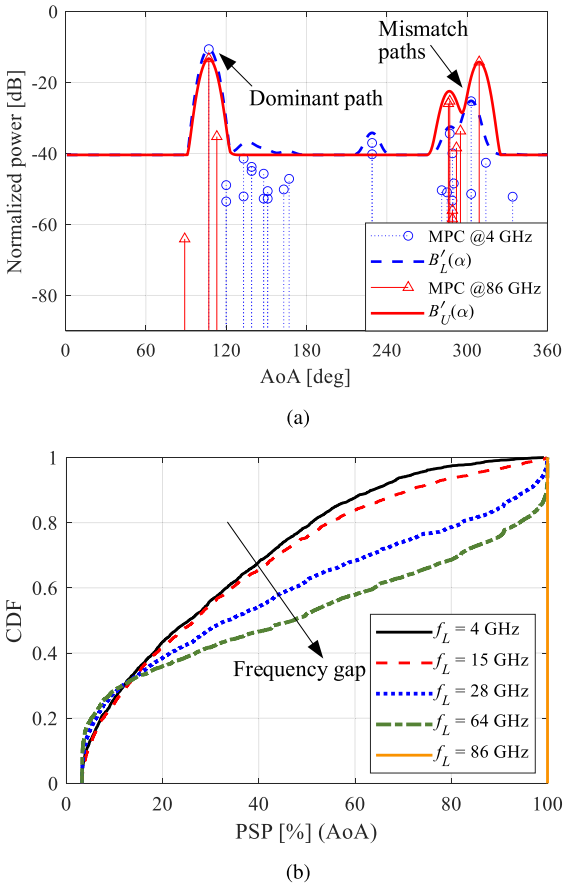

Fig. 7. (a) Normalized power patterns for PSP calculation (link 15). (b) Empirical CDF of the PSP metric with $f_U = 86$ GHz and $f_L = 4$, 15, 28, 64, 86 GHz.

2) Power Normalization: Both estimated spectra are normalized to the sum power of unity such that they can be interpreted as PDF. The normalized PAS at lower frequency is calculated as

$$B'_L(\alpha) = \frac{B_L(\alpha)}{\int B_L(\alpha)\mathrm{d}\alpha}. \tag{3}$$

$B'_U(\alpha)$ is similarly defined with respect to the upper-frequency PAS $B_U(\alpha)$. Fig. 7(a) depicts an example of normalized PAS $B'_L(\alpha)$ and $B'_U(\alpha)$ for link 15 at 4 and 86 GHz, respectively. Compared with the multipath shown in Fig. 5, the dominant directions of wave propagation in the azimuth plane are

aligned at the two frequencies, except for the path along the direction of 300°.

3) Total Variation Calculation: As defined in [32], the total variation distance between the normalized PASs is calculated as

$$d_{\text{tv}} = \frac{1}{2}\int |B'_L(\alpha) - B'_U(\alpha)|\text{d}\alpha. \tag{4}$$

$d_{\text{tv}} \in [0, 1]$ characterizes the cumulative difference of normalized PASs between two frequency bands. Conversely, the PSP is defined as

$$S = (1 - d_{\text{tv}}) \cdot 100\%. \tag{5}$$

The example link illustrated in Fig. 7(a) (and Fig. 5) yields PSP of 57.0%. We can observe how the deviation between $B'_L(\alpha)$ and $B'_U(\alpha)$ reduces the PSP value though the strongest path directions at both frequencies are perfectly aligned.

The empirical cumulative distribution function (CDF) of the PSP metric is collected over all 2875 links. To compare the spatial channel similarity across different frequency combinations, the CDF curves depicted in Fig. 7(b) are determined for five cases while keeping $f_U = 86$ GHz and choosing $f_L = 4$, 15, 28, 64, and 86 GHz. Since in this particular comparison, the beam pattern is unchanged across frequency bands, and we would expect to get the higher PSP, the smaller frequency gap $f_U - f_L$ we have. We can remark that the similarity percentage indeed increases, in general, with the decreasing frequency spacing between f_U and f_L and, ultimately, the similarity is always 100% at $f_U = f_L$, as anticipated. On the other hand, we can observe that this trend does not hold for all curves and even reverses when the PSP values are below 13%.

A low PSP value corresponds to significant difference between $B'_L(\alpha)$ and $B'_U(\alpha)$. This does not, however, necessarily mean high inaccuracy on beam directions obtained from the out-of-band channel, as can be seen in the analysis of the next section concerning the example link shown in Figs. 7(a) and 8(a). Moreover, the PSP metric only characterizes the overall channel gain difference over all directions in 360° azimuth plane, lacking the details at specific directions. Hence, the PSP metric can mainly be used to evaluate the channel similarity when multiband channels have a high spatial congruence. We can summarize that the PSP provides information on angular multipath, but it is not suitable for indicating the usefulness of out-of-band beam directions.

B. Beam Direction-Based Similarity Metric

To avoid the reverse results at different levels of channel similarity and to draw more practical conclusions, we define the other method with a focus on the collection of desired beam directions at the two frequencies. With this metric, we also consider the assumed antenna size constraints at different frequencies, rather than using the same beam pattern shown in Fig. 6.

Let us assume that low- and high-frequency radios and antenna systems operate equally at both link ends, where the lower-frequency antenna system presumably has a smaller electrical size, resulting in lower angular resolution and a larger beamwidth of the mainlobe. Next, we identify two sets of best beam directions at low and high frequencies, using the corresponding antenna beam patterns and propagation channel data. The sets of potential beam pointing angles in azimuth can be written as $\mathcal{A}_L = \{\theta_L | \theta_L \in [-\pi, \pi]\}$ and $\mathcal{A}_U = \{\theta_U | \theta_U \in [-\pi, \pi]\}$, respectively. Finally, we define a power ratio $R = \hat{P}_U(\mathcal{A}_L)/\hat{P}_U(\mathcal{A}_U)$ to measure how much potential channel gain is lost if the low-frequency beam direction information is used for high-frequency beam search instead of choosing its own channel information. Besides, we can count how many false, that is, completely useless directions are provided from the low frequency to the high frequency.

1) Determining Best Beam Directions: The sets of best beam directions $\mathcal{A}_L$ and $\mathcal{A}_U$ depend on the underlying radio channel, that is, propagation channel and antenna systems. By the best beam directions we mean a minimum set of directions for beam steering or antenna orientation, such that the potential multipath channel gains can be maximally[3] utilized. Different gain patterns $G_L(\Omega)$ and $G_U(\Omega)$ are employed to filter the raw PADPs according to (2). Fig. 8(a) shows an example of filtered PAS $B_L(\alpha)$ and $B_U(\alpha)$ for the link 15 using the 3GPP beam shape with the HPBW of 40° and 10° at 4 and 86 GHz, respectively. In [33], three methods are presented for identifying the desired directions. Here, the simplest method is utilized to choose the local maxima of $B(\alpha)$ with power threshold Δ_{th} of 15 dB. As shown in Fig. 8(a), in total, two best beam directions (the black squares) are selected in the lower band, while there are three directions selected in the higher band. One more direction can be detected in 295° at 86 GHz because of the narrower beam enabling to distinguish observable directions without angle ambiguities.

2) Calculating Power Ratio and False Direction Number: Based on the estimated sets of best beam directions, we consequently define the power ratio as the summation of power observed by the high-frequency antenna over different steering angle sets

$$R = \frac{\hat{P}_U(\mathcal{A}_L)}{\hat{P}_U(\mathcal{A}_U)} = \frac{\sum_{\theta_L \in \mathcal{A}_L} B_U(\theta_L)}{\sum_{\theta_U \in \mathcal{A}_U} B_U(\theta_U)}. \tag{6}$$

The ratio R determines how much power is collected in the high-frequency case using different beam direction sets. Large R indicates less power loss using low-frequency channel information and higher spatial similarity between radio channels at the two frequencies.

A direction $\alpha \in \mathcal{A}_L$ proposed from the low-frequency channel is interpreted as useless or "false" for high-frequency beam search if the high-frequency antenna does not collect any significant power when steered to that direction. More rigorously, we define the number of false directions as

$$N_f = \text{card}\left(\arg_{\alpha \in \mathcal{A}_L} \frac{B_U(\alpha)}{\max_{\alpha' \in \mathcal{A}_U} B_U(\alpha')} < \Delta_P\right) \tag{7}$$

where card$(\cdot)$ denotes the cardinality of a set and Δ_P is a power threshold (e.g., −30 dB). The number of these false

[3]As is well known, the optimal selection of beam directions depends on transceiver architectures, MIMO transmission schemes, beamforming strategies, and so on and hence cannot be exactly determined without such a priori knowledge.

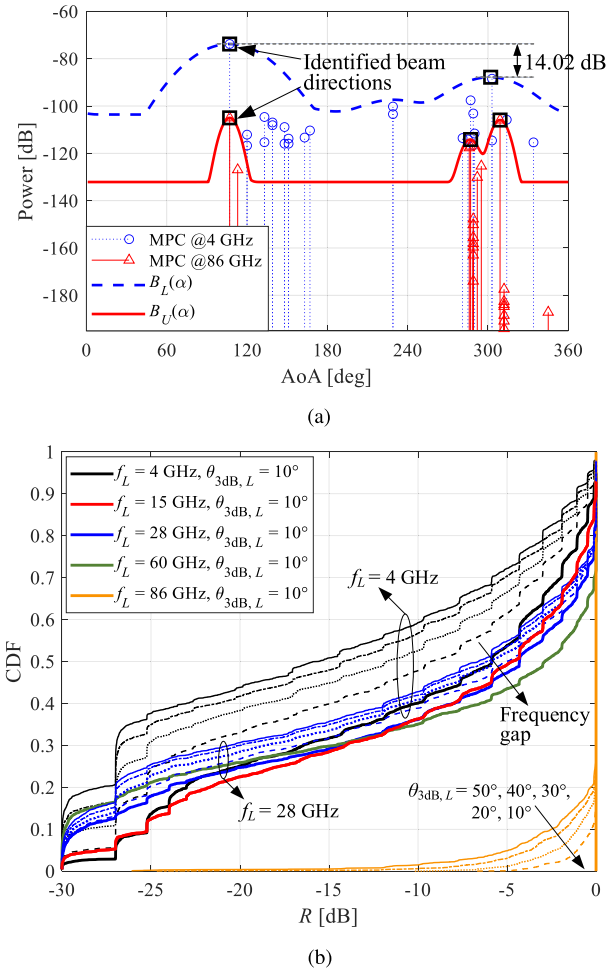

Fig. 8. (a) Original discrete PAS and filtered power patterns (link 15). (b) Empirical CDF of the power ratios R under different f_L and $\theta_{3\ \mathrm{dB},L}$ combinations with respect to $f_U = 86$ GHz and $\theta_{3\ \mathrm{dB},U} = 10°$. Line types denote $\theta_{3\ \mathrm{dB},L}$ values: solid 50°, dash dotted 40°, dotted 30°, dashed 20°, and solid bold 10°.

directions can be counted per link, and their empirical probability distribution over all links can be extracted. Likewise, the cardinality of sets $\mathcal{A}_L$ and $\mathcal{A}_U$ can be collected and their corresponding PDF can be extracted. For the case shown in Fig. 8(a), the corresponding R and N_f are, respectively, -2.02 dB and 0, while if Δ_{th} was selected as 10 dB, R and N_f were -2.86 dB and 0, respectively.

It is evident that the power ratio R depends on both the similarity of discrete PASs $P_L(\Omega)$ and $P_U(\Omega)$, as well as the shapes of antenna patterns $G_L(\Omega)$ and $G_U(\Omega)$. For assessing the proposed method, we determine the CDF of R while keeping $f_U = 86$ GHz and the HPBW of G_U as 10°, and taking selected combinations of $f_L = 4$, 15, 28, 64, and 86 GHz and the HPBW of G_L as 50°, 40°, 30°, 20°, and 10°. We can observe from Fig. 8(b) that R almost monotonically increases, that is, the power loss at high frequency by using the low-frequency spatial channel information becomes smaller, as both the frequency gap and the HPBW difference decrease. The highest loss is 30 dB, which is determined by the peak-to-minimum gain ratio of the selected 3GPP beam shapes shown in Fig. 6. As expected, when the same frequencies (i.e., $f_L = f_U$) and HPBW are selected, the power loss is 0 dB over all links (see the orange bold solid line). Moreover, it seems that the beamwidth has an even stronger impact on channel similarity than the frequency difference. For example, the power ratio is much larger when using the spatial channel information at $f_L = 4$ GHz with $\theta_{3\ \mathrm{dB},L} = 10°$ in comparison with the results at $f_L = 28$ GHz with $\theta_{3\ \mathrm{dB},L} = 40°$.

IV. Results and Discussion

In the following, we evaluate the feasibility of out-of-band spatial channel information for mm-wave beam search based on the previously described multiband propagation data, using the beam direction-based similarity metric defined in Section III-B. We choose upper/lower frequency combinations 4/86 and 28/100 GHz for the simulation- and measurement-based analyses, respectively. Instead of the ideal 3GPP beam pattern, we utilize more practical beam patterns of uniform linear arrays (ULAs) with different element number N at different frequencies.

A. Validation With Dual-Band LOS Measurements

The 28- and 84-GHz measured PASs are filtered with the beam patterns of half-wavelength spaced ULAs with four and eight elements, respectively. Here, four and eight are typical numbers of elements in azimuth for commercial mm-wave systems. Beam patterns $G_L(\Omega)$ and $G_U(\Omega)$ of arrays are defined for $\Omega \in [-\pi/2, \pi/2]$ bore-sight half-plane with all-zero phasing, while the back half-plane $\Omega \in [-\pi, -\pi/2] \vee [\pi/2, \pi]$ is set to constant -60 dB gain. As shown in Fig. 9(a), the HPBW of mainlobes are 26.2° and 12.8° for $G_L(\Omega)$ and $G_U(\Omega)$, respectively. The filtering of PAS by beam patterns is performed by rotating the patterns, not by setting various steering angles and using DFT weights, as would be the normal procedure with phased arrays. This approach is chosen since propagation paths are distributed over a wide sector of angles and in turn, we can remove the impact of ULA orientation on realized beam patterns.

The two methods proposed in [33] for identifying beam directions are used. With method 1 (M1), each local maximum of $B(\alpha)$ within $\Delta_{\mathrm{th}} = 10$ dB range from the global maximum is selected, and for method 2 (M2), the same 10 dB range is used, but instead of local maxima the directions are selected based on the power and computational correlation between corresponding channel frequency responses.

Fig. 9(b) shows a multipath of an example link in the corridor environment. It can be observed that one beam direction at 28 GHz and two at 100 GHz can be extracted using M2 and the corresponding power loss is 0.91 dB ($=-R$ dB). When using M1, only one beam direction can be extracted at both frequencies and the resulting power loss is 1.55 dB. In a link of the entrance hall, depicted in Fig. 9(c), three beam directions can be detected at two frequency bands with power losses 0.13 and 0.09 dB using M1 and M2, respectively. The number of false directions N_f is zero in all mentioned cases. In general, M2 can estimate more possible beam directions than M1 [33], which leads to smaller power loss. This is the

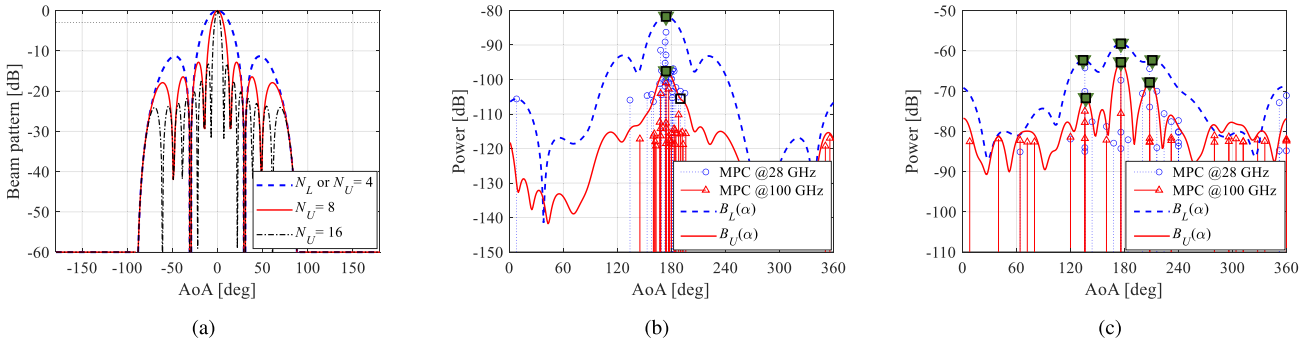

(a) (b) (c)

Fig. 9. (a) Beam patterns of 4-, 8-, and 16-element ULAs. Measurement-based analysis of spatial channel similarity between 28 and 100 GHz in (b) indoor corridor and (c) entrance hall with (N_L, N_U) = (4, 8). The green inverted triangles and black squares in (b) and (c) represent the identified beam directions using M1 and M2, respectively.

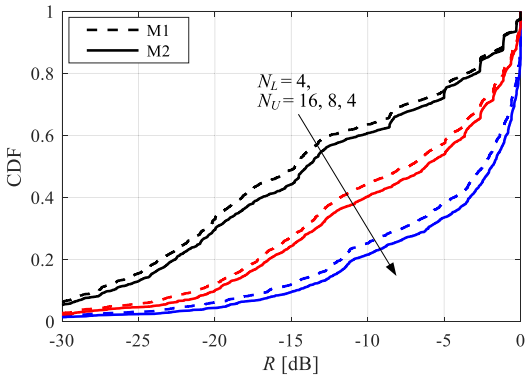

Fig. 10. Empirical CDF of the power ratio metric based on ray-tracing simulation data. Black, red, and blue curves denote $N_U = 16$, 8, and 4 cases, respectively.

trend, especially when using a narrower beam pattern to filter the propagation channel. Measurement-based results show that our proposed metric performs well in LOS scenarios between two bands with tens of gigahertz frequency gap, especially when the more advanced beam identification method, that is, M2 is adopted. We can observe that in LOS condition, the angular profile of propagation channels is similar, the out-of-band information is useful, and the power loss due to incorrect beam directions at the upper frequency is minor.

B. Feasibility Study With Statistical Analysis

The evaluations of Section III-B show a significant impact of antenna HPBW on the measure of spatial channel similarity across different frequencies using ideal 3GPP beam patterns. Here, we promote statistical analysis of radio channel similarity based on 4- and 86-GHz ray-tracing data, where ULA beam patterns are used to filter propagation channels. At f_L, we use similar 4-element ULA as in the previous section, while at f_U, we evaluate 4-, 8-, and 16-element ULAs. All three beam patterns are illustrated in Fig. 9(a).

CDF curves of power ratios R over all 2875 NLOS links assuming different beam patterns and beam direction estimation methods are shown in Fig. 10, as well as their statistics in Table III. As the first observation, we can notice that losses R are substantially higher when compared to the LOS examples of the previous section. Furthermore, we can observe that the CDF curves for M2 can provide slightly higher values of R compared with M1. The values of R are also sensitive to the beamwidth, that is, the ULA aperture. When using the direction information of the 4-GHz channel to aid in the 86-GHz beam search, at worst 2.27-, 7.31-, and 14.77-dB power losses are introduced in 50% of cases when 4-, 8-, and 16-element ULAs are employed in higher frequency bands, respectively.

While R indicates whether all significant directions are included in 86-GHz beam steering, it is also important to consider how many false directions are indicated by the 4-GHz $\mathcal{A}_L$. Fig. 11 depicts the PDFs of both the number of false directions N_f and all identified beam directions within $\mathcal{A}_L$. We have set in this analysis Δ_P of (7) as -30 dB. As expected, less false directions are introduced if the same beam patterns are used at 4 and 86 GHz.

With simple reasoning, one can understand that statistically R and N_f must be proportional. Namely, if the criteria to find beam directions at f_L is loosened, the more directions are provided to f_U in the set $\mathcal{A}_L$ (this is shown in [33]) and the higher ratio R is obtained, but consequently, N_f is increased as well. In other words, the higher number of false directions we can tolerate, the lower power loss we can achieve when solely following the out-of-band directions. Hence, there is a tradeoff between R and N_f when measuring the degree of spatial similarity between low- and high-frequency radio channels. It is remarkable that N_f is less than or equal to one in most of the cases (>80%), meaning that spatial channel similarity between 4- and 86-GHz radio channels can be exploited to realize coarse estimation of mm-wave beam directions without the noticeable effort of searching around false directions.

C. Analysis of Nonsuccessful Cases

There is a good share of cases where the 4-GHz beam information provides an adequate basis for the 86-GHz beam directions as the statistical analysis indicates. A good example is the link 15 shown in Fig. 8(a) with $N_f = 0$ and $R = -2.86$ dB. However, there is another set of links where a low-frequency radio channel observed by a lower-resolution antenna provides no useful information for an 86-GHz beam search. In these cases, there is often a strong path at the low frequency, which is not present or is only weak at the high

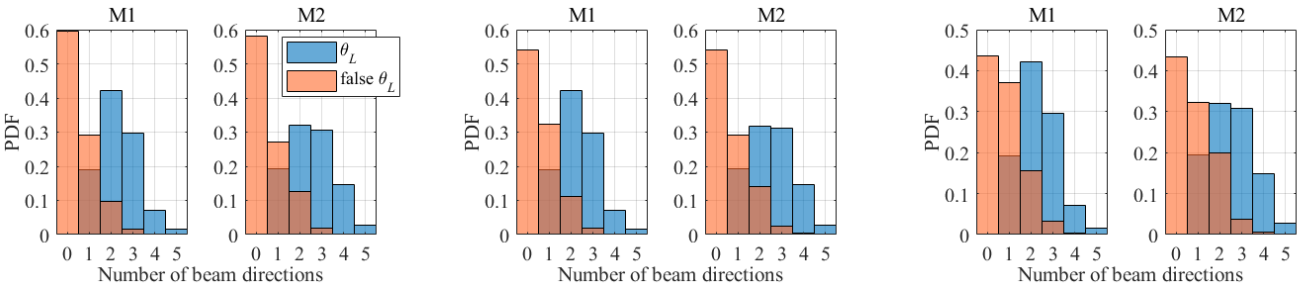

Fig. 11. Empirical PDF of the number of false directions and all extracted beam directions using 4-GHz out-of-band spatial channel information with the (N_L, N_U) of (a) (4, 4), (b) (4, 8), and (c) (4, 16).

TABLE III

STATISTICS OF POWER RATIOS R AND NUMBER OF FALSE DIRECTIONS N_f UNDER DIFFERENT ANTENNA CONFIGURATIONS WITH Δ_{th}=10 DB

(N_L, N_U)		(4, 4)		(4, 8)		(4, 16)	
Method		M1	M2	M1	M2	M1	M2
R [−dB]	10%	16.49	14.7	21.14	20.00	27.58	26.77
	50%	2.27	1.88	7.31	6.20	14.77	14.00
	90%	0	0	0.26	0.21	1.13	1.12
N_f [%]	= 0	59.44	58.05	54.09	54.16	43.58	43.30
	≤1	89.62	85.18	86.47	83.17	80.77	75.48

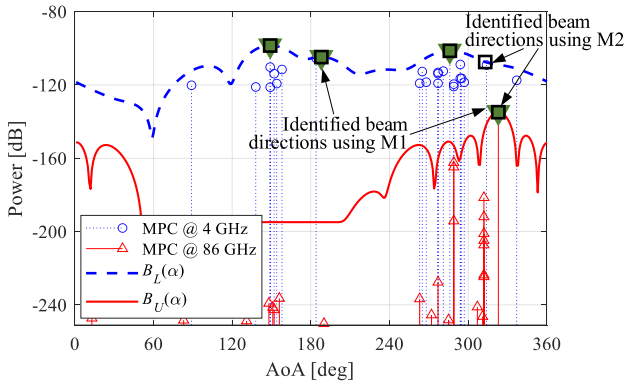

Fig. 12. Original discrete PAS and filtered power patterns (Link 19).

frequency. We do not have an exhaustive analysis of all these incidences, but in some cases, the root cause is diffraction and in some other cases, the path is more severely shadowed by an obstacle at a high frequency. An example of such link is shown in Fig. 12 with $(N_L, N_U) = (4, 8)$, where $N_f = 2$ (with M1) and $R = -16.15$ dB. There, the strong paths of 4-GHz channels do not coincide with those of 86-GHz channels, or more precisely, there is only a single dominant propagation path at 84 GHz and it is not present at 4 GHz.

Overall, the spatial similarity of propagation channel at different RFs can be assessed with the beam domain perspective. The out-of-band spatial channel information-aided mm-wave beam search strategy is expected to perform well for the links containing strong and dominant paths, while multipath scattering components easily lead to an angle mismatch between two well-separated frequency bands. The analysis of the measurement- and ray-tracing-based results in LOS and NLOS scenarios, respectively, supports the expectation.

V. CONCLUSION

In this article, we analyze an extensive set of multiband propagation data and propose two metrics to evaluate the spatial similarity of radio channels across different frequencies. We conduct a feasibility study of out-of-band spatial information-aided mm-wave beam search from a radio channel similarity perspective. The first metric, the PAS similarity percentage, was found nonsatisfying. The other, the proposed beam direction-based spatial similarity metric, compares the potential angular directions estimated from radio channels and provides the power loss and the number of false directions introduced by solely using out-of-band information. Moreover, we perform a quantitative analysis of both point cloud ray-tracing and measured data with respect to the metric. The results indicate that the usability of low-frequency radio channel information for high-frequency beam search evidently depends on many choices, for example, of assumed angular resolutions and beam patterns of antennas, of the frequency gaps, of the criterion to select beam directions, and of accepting false directions. Overall, it seems practical to leverage available spatial channel information from lower-frequency bands to aid mm-wave beam steering from the radio channel point of view, but it should not rely on out-of-band information blindly. For example, among the evaluated NLOS links, in 50% of cases, one would lose 6.2 dB or less power, if 86-GHz beam steering with eight-element ULA solely follows the out-of-band direction set $\mathcal{A}_L$ obtained from the 4-GHz radio channel with four-element ULA, instead of the in-band direction set $\mathcal{A}_U$.

For future work, the need for high-efficient beam search strategies becomes even more urgent in upper mm-wave and terahertz bands (e.g., 100–300 GHz), since narrower beams increase the complexity of beam management under possible hardware limitations with potential less flexibility. It would be of interest to include more statistical performance analysis of our proposed channel similarity metric with exhaustive directional propagation measurement campaigns. Moreover, developing a sophisticated metric for dynamic channel similarity measures is also an interesting research direction.

ACKNOWLEDGMENT

The authors would like to thank their colleague Mr. Yejian Lyu from Aalborg University for his valuable support in channel measurements and parameter estimation.

REFERENCES

[1] H. Tataria, M. Shafi, A. F. Molisch, M. Dohler, H. Sjöland, and F. Tufvesson, "6G wireless systems: Vision, requirements, challenges, insights, and opportunities," *Proc. IEEE*, vol. 109, no. 7, pp. 1166–1199, Jul. 2021.

[2] A. Pärssinen et al., "White paper on RF enabling 6G—Opportunities and challenges from technology to spectrum," 6G Res. Visions Univ. Oulu, Oulu, Finland, White Paper 13, Apr. 2021. [Online]. Available: http://urn.fi/urn:isbn:9789526228419

[3] K. Rikkinen, P. Kyosti, M. E. Leinonen, M. Berg, and A. Parssinen, "THz radio communication: Link budget analysis toward 6G," *IEEE Commun. Mag.*, vol. 58, no. 11, pp. 22–27, Nov. 2020.

[4] G. R. MacCartney and T. S. Rappaport, "Rural macrocell path loss models for millimeter wave wireless communications," *IEEE J. Sel. Areas Commun.*, vol. 35, no. 7, pp. 1663–1677, Jul. 2017.

[5] P. Zhang, B. Yang, C. Yi, H. Wang, and X. You, "Measurement-based 5G millimeter-wave propagation characterization in vegetated suburban macrocell environments," *IEEE Trans. Antennas Propag.*, vol. 68, no. 7, pp. 5556–5567, Jul. 2020.

[6] J. Ko et al., "Millimeter-wave channel measurements and analysis for statistical spatial channel model in in-building and urban environments at 28 GHz," *IEEE Trans. Wireless Commun.*, vol. 16, no. 9, pp. 5853–5868, Jun. 2017.

[7] P. Z. Zhang, H. M. Wang, and W. Hong, "Radio propagation measurements and cluster-based analysis for 5G millimeter-wave cellular systems in dense urban environments," *Frontiers Inf. Technol. Electron. Eng.*, vol. 22, no. 4, pp. 471–487, Apr. 2021.

[8] M. Shafi et al., "Microwave vs. millimeter-wave propagation channels: Key differences and impact on 5G cellular systems," *IEEE Commun. Mag.*, vol. 56, no. 12, pp. 14–20, Dec. 2018.

[9] V. Raghavan, J. Cezanne, S. Subramanian, A. Sampath, and O. Koymen, "Beamforming tradeoffs for initial UE discovery in millimeter-wave MIMO systems," *IEEE J. Sel. Topics Signal Process.*, vol. 10, no. 3, pp. 543–559, Apr. 2016.

[10] M. Giordani, M. Polese, A. Roy, D. Castor, and M. Zorzi, "A tutorial on beam management for 3GPP NR at mmWave frequencies," *IEEE Commun. Surveys Tuts.*, vol. 21, no. 1, pp. 173–196, 1st Quart., 2019.

[11] N. Gonzalez-Prelcic, A. Ali, V. Va, and R. W. Heath Jr., "Millimeter-wave communication with out-of-band information," *IEEE Commun. Mag.*, vol. 55, no. 12, pp. 140–146, Dec. 2017.

[12] A. Ali, N. González-Prelcic, and R. W. Heath, "Millimeter wave beam-selection using out-of-band spatial information," *IEEE Trans. Wireless Commun.*, vol. 17, no. 2, pp. 1038–1052, Feb. 2018.

[13] D. Dupleich et al., "Multi-band propagation and radio channel characterization in street canyon scenarios for 5G and beyond," *IEEE Access*, vol. 7, pp. 160385–160396, 2019.

[14] *Study on Channel Model for Frequencies From 0.5 to 100 GHz*, Standard TR 38.901, 3GPP, Tech. Rep. V14.1.1, Jul. 2017.

[15] B. Peng, K. Guan, S. Rey, and T. Kürner, "Power-angular spectra correlation based two step angle of arrival estimation for future indoor terahertz communications," *IEEE Trans. Antennas Propag.*, vol. 67, no. 11, pp. 7097–7105, Nov. 2019.

[16] W. Fan, I. Carton, J. Ø. Nielsen, K. Olesen, and G. F. Pedersen, "Measured wideband characteristics of indoor channels at centimetric and millimetric bands," *EURASIP J. Wireless Commun. Netw.*, vol. 2016, no. 1, pp. 1–13, Dec. 2016.

[17] P. Zhang, J. Li, H. Wang, H. Wang, and W. Hong, "Indoor small-scale spatiotemporal propagation characteristics at multiple millimeter-wave bands," *IEEE Antennas Wireless Propag. Lett.*, vol. 17, no. 12, pp. 2250–2254, Dec. 2018.

[18] P. Zhang, J. Li, H. Wang, and X. You, "Millimeter-wave space-time propagation characteristics in urban macrocell scenarios," in *Proc. IEEE Int. Conf. Commun. (ICC)*, May 2019, pp. 1–6.

[19] Y. Lyu, P. Kyösti, and W. Fan, "Sub-THz VNA-based channel sounder structure and channel measurements at 100 and 300 GHz," in *Proc. IEEE 32nd Annu. Int. Symp. Pers., Indoor Mobile Radio Commun. (PIMRC)*, Sep. 2021, pp. 1–5.

[20] S. L. H. Nguyen et al., "On the frequency dependency of radio channel's delay spread: Analyses and findings from mmMAGIC multi-frequency channel sounding," in *Proc. 12th Eur. Conf. Antennas Propag. (EuCAP)*, Apr. 2018, pp. 1–5.

[21] mmMAGIC D2.2. (2017). *Measurement Results and Final mmMAGIC Channel Models*. Deliverable D2.2, Ver. 1. [Online]. Available: https://5g-mmmagic.eu/results/

[22] C. Yi, P. Zhang, H. Wang, and W. Hong, "Multipath similarity index measure across multiple frequency bands," *IEEE Wireless Commun. Lett.*, vol. 10, no. 8, pp. 1677–1681, Aug. 2021.

[23] P. Koivumäki, G. Steinböck, and K. Haneda, "Impacts of point cloud modeling on the accuracy of ray-based multipath propagation simulations," *IEEE Trans. Antennas Propag.*, vol. 69, no. 8, pp. 4737–4747, Aug. 2021.

[24] J. Järveläinen, K. Haneda, and A. Karttunen, "Indoor propagation channel simulations at 60 GHz using point cloud data," *IEEE Trans. Antennas Propag.*, vol. 64, no. 10, pp. 4457–4467, Oct. 2016.

[25] Zoller+Fröhlich GmbH. (2010). *Z+F IMAGER 5006h*. [Online]. Available: https://zf-usa.com/wp-content/uploads/2011/10/IMAGER5006hbrochure.pdf

[26] J. Vehmas, J. Jarvelainen, S. Le Hong Nguyen, R. Naderpour, and K. Haneda, "Millimeter-wave channel characterization at Helsinki airport in the 15, 28, and 60 GHz bands," in *Proc. IEEE 84th Veh. Technol. Conf. (VTC-Fall)*, Sep. 2016, pp. 1–5.

[27] J. Järvelainen, S. L. H. Nguyen, K. Haneda, R. Naderpour, and U. T. Virk, "Evaluation of millimeter-wave line-of-sight probability with point cloud data," *IEEE Wireless Commum. Lett.*, vol. 5, no. 3, pp. 228–231, Jun. 2016.

[28] P. Koivumäki, A. F. Molisch, and K. Haneda, "Line-of-sight probability in cluttered urban microcells: Analyses using Poisson point process and point cloud," *IEEE Trans. Antennas Propag.*, vol. 70, no. 3, pp. 2161–2173, Mar. 2022.

[29] A. W. Mbugua, W. Fan, K. Olesen, X. Cai, and G. Frølund Pedersen, "Phase-compensated optical fiber-based ultrawideband channel sounder," *IEEE Trans. Microw. Theory Techn.*, vol. 68, no. 2, pp. 636–647, Feb. 2020.

[30] Y. Lyu, A. W. Mbugua, K. Olesen, P. Kyösti, and W. Fan, "Design and validation of the phase-compensated long-range sub-THz VNA-based channel sounder," *IEEE Antennas Wireless Propag. Lett.*, vol. 20, no. 12, pp. 2461–2465, Dec. 2021.

[31] M. Li, F. Zhang, Y. Ji, and W. Fan, "Virtual antenna array with directional antennas for millimeter-wave channel characterization," *IEEE Trans. Antennas Propag.*, vol. 70, no. 8, pp. 6992–7003, Aug. 2022.

[32] P. Kyösti, L. Hentilä, W. Fan, J. Lehtomäki, and M. Latva-Aho, "On radiated performance evaluation of massive MIMO devices in multiprobe anechoic chamber OTA setups," *IEEE Trans. Antennas Propag.*, vol. 66, no. 10, pp. 5485–5497, Oct. 2018.

[33] P. Kyosti, M. F. D. Guzman, K. Haneda, N. Tervo, and A. Parssinen, "How many beams does sub-THz channel support?" *IEEE Antennas Wireless Propag. Lett.*, vol. 21, no. 1, pp. 74–78, Jan. 2022.

Pekka Kyösti received the M.Sc. degree in mathematics and the D.Sc. degree (Hons.) in communications engineering from the University of Oulu, Oulu, Finland, in 2000 and 2018, respectively.

From 1998 to 2002, he was with Nokia Networks; from 2002 to 2016, he was with Elektrobit/Anite; and since 2016, he has been with Keysight Technologies Finland Oy (part-time), Oulu. Since 2002, he has also been involved in radio channel measurements, estimation, and modeling. From 2008 to 2012, he developed methods for MIMO over-the-air testing. He has acted in contributor and task leader roles in many past research projects, such as Wireless World Initiative New Radio (WINNER) (I, II, +) and Mobile and wireless communications Enablers for the Twenty-twenty Information Society (MEITS). He is currently a Research Director of the 6G Flagship Program and a Docent (Adjunct Professor) with the Centre for Wireless Communications (CWC), University of Oulu, and a Senior Specialist with Keysight Technologies Finland Oy. His research interests include radio channel characterization for 6G systems, channel modeling, and over-the-air emulation for 5G systems.

Dr. Kyösti has contributed to channel modeling on many standardizations, such as International Telecommunication Union - Radio technology (ITU-R), 3rd Generation Partnership Program (3GPP) (Radio Access Networks 1/2 (RAN1/2), RAN4), CTIA, and IEEE 802. He has been a Guest Editor for the Special Issue of *IET Microwaves, Antennas & Propagation*, IEEE JOURNAL ON SELECTED AREAS IN COMMUNICATIONS, IEEE ACCESS, IEEE OPEN JOURNAL OF ANTENNAS AND PROPAGATION, and IEEE TRANSACTIONS ON ANTENNAS AND PROPAGATION, from 2019 to 2024.

Peize Zhang (Member, IEEE) received the B.S. degree from the Beijing University of Posts and Telecommunications, Beijing, China, in 2015, the M.S. degree from the China Academy of Telecommunications Technology, Beijing, in 2018, and the Ph.D. degree from Southeast University, Nanjing, China, in 2022, all in electrical engineering.

From 2016 to 2018, he was a Research Assistant with the China Academy of Information and Communications Technology, Beijing. In 2021, he was also a visiting Ph.D. student with the Université Catholique de Louvain, Leuven-la-Neuve, Belgium. Since 2022, he has been a Postdoctoral Researcher in the 6G Flagship Program with the Centre for Wireless Communications (CWC), University of Oulu, Oulu, Finland. His current research interests include propagation, deployment, and performance issues of millimeter-wave/THz communication systems.

Aarno Pärssinen (Senior Member, IEEE) received the M.Sc. degree, the Licentiate degree in technology, and the D.Sc. degree in electrical engineering from the Helsinki University of Technology, Espoo, Finland, in 1995, 1997, and 2000, respectively.

From 1994 to 2000, he was with the Electronic Circuit Design Laboratory, Helsinki University of Technology, working on direct conversion receivers and subsampling mixers for wireless communications. In 1996, he was a Research Visitor at the University of California at Santa Barbara, Santa Barbara, CA, USA. From 2000 to 2011, he was with the Nokia Research Center, Helsinki, Finland. From 2009 to 2011, he served as a member of Nokia CEO Technology Council. From 2011 to 2013, he was at Renesas Mobile Corporation, Helsinki, working as a Distinguished Researcher and an RF Research Manager. From October 2013 to September 2014, he was an Associate Technical Director at Broadcom, Helsinki. Since September 2014, he has been with the Centre for Wireless Communications, University of Oulu, Oulu, Finland, where he is currently a Professor. He leads the devices and circuits research area in the 6G flagship program financed by the Academy of Finland, Helsinki. He has authored or coauthored one book, two book chapters, more than 200 international journals and conference papers, and holds several patents. His research interests include wireless systems, transceiver architectures for wireless communications with special emphasis on RF, and analog integrated circuit and system design.

Dr. Pärssinen has served as a member of the Technical Program Committee of the International Solid-State Circuits Conference from 2007 to 2017. He was a recipient of European Microwave Price on the best paper of the European Microwave Conference in 2020. He is also one of the original contributors to Bluetooth low energy extension, now called BT LE. He was the Chair of the European Regional Committee from 2012 to 2013 and the Wireless Sub-Committee from 2014 to 2017. He has served as a Solid-State Circuits Society Representative for IEEE 5G Initiative from 2015 to 2019.

Katsuyuki Haneda (Member, IEEE) is currently an Associate Professor with the Aalto University School of Electrical Engineering, Espoo, Finland. His current research activity covers high-frequency radios such as millimeter-waves and beyond and wireless for medical and smart-city applications.

Dr. Haneda has authored or coauthored a number of the best paper and student paper awards in the IEEE Vehicular Technology Conference and European Conference on Antennas and Propagation, among others. He also received the R. W. P. King Paper Award of the IEEE TRANSACTIONS ON ANTENNAS AND PROPAGATION in 2021, together with Dr. Usman Virk. He was the Co-Chair of a disciplinary working group on radio channels in European COST Actions CA15104 Inclusive Radio Communication Networks for 5G and beyond (IRACON) from 2016 to 2020. He is the Technical Program Committee Co-Chair of the 17th European Conference on Antennas and Propagation (EuCAP 2023), Florence, Italy. He was an Associate Editor of the IEEE TRANSACTIONS ON ANTENNAS AND PROPAGATION from 2012 to 2016 and an Editor of the IEEE TRANSACTIONS ON WIRELESS COMMUNICATIONS from 2013 to 2018. He was a Guest Editor for the Special Issue on Antennas and Propagation Aspects of In-Band Full-Duplex Applications and the Special Issue on Artificial Intelligence in Radio Propagation for Communications of the IEEE TRANSACTIONS ON ANTENNAS AND PROPAGATION in 2021 and 2022, respectively. He is also a Guest Editor for the forthcoming Special Section on Sub-THz and THz Radio Propagation: Measurements and Characterization of the IEEE OPEN JOURNAL OF ANTENNAS AND PROPAGATION.

Pasi Koivumäki (Member, IEEE) received the M.Sc. (Tech.) degree (Hons.) from the Aalto University School of Electrical Engineering, Espoo, Finland, in 2017, where he is currently pursuing the D.Sc. (Tech.) degree in radio engineering.

His current research interests include multiband radio channel measurements and simulations and modeling focusing on mm-wave frequencies for 5G systems and beyond. His particular interests lie in ray-launching and ray-tracing algorithms for propagation and channel modeling in urban environments of future smart cities and their combined effects on cellular coverage and quality of service.

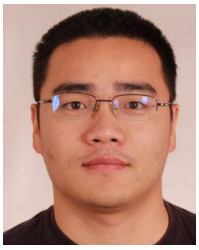

Wei Fan (Senior Member, IEEE) received the B.Eng. degree from the Harbin Institute of Technology, Harbin, China, in 2009, the dual master's degree (Hons.) from the Politecnico di Torino, Turin, Italy, and the Grenoble Institute of Technology, Grenoble, France, in 2011, and the Ph.D. degree from Aalborg University, Aalborg, Denmark, in 2014.

From February 2011 to August 2011, he was with Intel Mobile Communications, Aalborg, as a Research Intern. He conducted a three-month internship at Anite Telecoms oy (now Keysight Technologies), Oulu, Finland, in 2014. He is currently an Associate Professor with Aalborg University, heading the "wireless channel and over-the-air testing" research group and a docent with the University of Oulu, Oulu. His main research interests include over-the-air testing of multiple antenna systems, radio channel sounding, modeling and emulation, and antenna array signal processing.